EDGE ARTICLE

Check for updates

Using internal electrostatic fields to manipulate the valence manifolds of copper complexes†

Alexander B. Weberg, Samuel P. McCollom, Laura M. Thierer, Michael R. Gau, Patrick J. Carroll and Neil C. Tomson ID *

A series of tetradentate tris(phosphinimine) ligands ($^{R3}P_3$tren) was developed and bound to Cu^I to form the trigonal pyramidal, C_{3v}-symmetric cuprous complexes [$^{R3}P_3$tren-Cu][BAr$^F_4$] (1^{PR3}) (PR$_3$ = PMe$_3$, PMe$_2$Ph, PMePh$_2$, PPh$_3$, PMe$_2$(NEt$_2$), BAr$^F_4$ = B(C$_6$F$_5$)$_4$). Electrochemical studies on the Cu^I complexes were undertaken, and the permethylated analog, 1^{PMe3}, was found to display an unprecedentedly cathodic Cu^I/Cu^{II} redox potential (−780 mV *vs.* Fc/Fc$^+$ in isobutyronitrile). Elucidation of the electronic structures of 1^{PR3} *via* density functional theory (DFT) studies revealed atypical valence manifold configurations, resulting from strongly σ-donating phosphinimine moieties in the *xy*-plane that destabilize 2*e* (d$_{xy}$/d$_{x^2−y^2}$) orbital sets and uniquely stabilized a_1 (d$_{z^2}$) orbitals. Support is provided that the a_1 stabilizations result from intramolecular electrostatic fields (ESFs) generated from cationic character on the phosphinimine moieties in $^{R3}P_3$tren. This view is corroborated *via* 1-dimensional electrostatic potential maps along the *z*-axes of 1^{PR3} and their isostructural analogues. Experimental validation of this computational model is provided upon oxidation of 1^{PMe3} to the cupric complex [$^{Me3}P_3$tren-Cu][OTf]$_2$ (2^{PMe3}), which displays a characteristic Jahn−Teller distortion in the form of a see-saw, pseudo-C_s-symmetric geometry. A systematic anodic shift in the potential of the Cu^I/Cu^{II} redox couple as the steric bulk in the secondary coordination sphere increases is explained through the complexes' diminishing ability to access the ideal C_s-symmetric geometry upon oxidation. The observations and calculations discussed in this work support the presence of internal electrostatic fields within the copper complexes, which subsequently influence the complexes' properties *via* a method orthogonal to classic ligand field tuning.

Introduction

Frontier orbitals are at the heart of chemical reactivity. Many reactions can be simplified to an interaction between the highest occupied molecular orbital (HOMO) of one species and the lowest unoccupied molecular orbital (LUMO) of another. Deliberate control of the frontier orbital energies is therefore crucial to facilitating desirable chemistry and preventing side reactions. The development of new tools for manipulating valence manifolds may be envisioned to support the creation of unique catalysts, photochemical reagents, and separations technologies.

The active site architectures of metalloenzymes have historically provided much inspiration to this task. Current design principles such as metal choice, active-site geometries, use of pH-responsive ligands, incorporation of hydrogen-bonding moieties into secondary coordination spheres, and

Roy and Diana Vagelos Laboratories, Department of Chemistry, University of Pennsylvania, 231 South 34th Street, Philadelphia, Pennsylvania 19104, USA. E-mail: tomson@upenn.edu

the use of multinuclear clusters have all received inspiration or analogy in bioinorganic chemistry. An underexplored concept from enzymology is the use of properly aligned electric fields for reaction site engineering. As described in detail below, the application of this burgeoning method to transition metal chemistry provides a promising new avenue for exerting precise control over the electronic structures and reactivity profiles of homogeneous systems. Inasmuch as orbital energies reflect the energy of a single electron experiencing the waveform and potential energy environment of the orbital, the structure of the valence manifold should be susceptible to the application of a properly aligned electrostatic field. The general importance of local electrostatic fields to enzymatic function was originally proposed by Warshel[1] and has since been studied in detail by Boxer.[2–4] Accumulated work in this area has even been used in support of the argument that electrostatic effects may be general to enzyme catalysis.[3–5]

Research outside of the biochemical field has investigated the effects of electrostatic fields on the electronic structure and reactivity of various materials. This work has included (i) the use of bulk, homogeneous electric fields,[6–8] (ii) the study of anion effects on reaction selectivity,[9] (iii) the study of electrostatic stabilization of *in situ*-generated radical species,[10–14] and (iv) in-

depth computational studies on reaction barrier (de)stabilization of organic molecules bearing charged functional groups.[15–20] Limited examples are known of transition metal complexes that use oriented internal electrostatic fields to tune the properties of the system. The Tolman group reported cupric hydroxide compounds bound by NNN pincer-type bis(carboxamide)pyridine ligands, wherein charged residues were incorporated at the *para* positions of the carboxamide aryl rings.[21] A shift of ~0.3 V in the Cu^{II}/Cu^{III} redox couple was observed upon switching between substitution of a cationic group ($-NMe_3^+$) with an anionic group ($-SO_3^-$), implicating a through-space electrostatic effect on the potential of this redox couple (Fig. 1a). Similarly, using a salen-based ligand containing a crown-ether moiety, Yang and coworkers showed a systematic anodic shift in the Co^{II}/Co^{III} redox couples across a series of Co^{II} complexes as alkali and alkaline earth metals were tethered in the secondary coordination sphere (Fig. 1b).[22] These anodic shifts correlated with the strength of electrostatic fields emanating from the redox-innocent metal, as opposed the

Lewis acidity of these metals. Impressively, securing redox-innocent metals in the crown-ether pocket of this ligand was also shown to improve aerobic oxidation catalysis with Fe^{III} complexes[23] and promote stability across a series of Mn^V-nitride complexes.[24]

Success in this field has also been realized through incorporation of charges into the secondary coordination spheres of heme-based complexes. Savéant published an elegantly designed series of iron/porphyrin-based CO_2 electro-reduction catalysts, wherein charged functional groups were placed at different distances from the catalyst active site.[25] In this case, a dramatic decrease in overpotential was observed when the cationic charges were placed in closest proximity to the CO_2 binding site (Fig. 1c). Mayer reported this same complex to be a fast and efficient catalyst for the oxygen reduction reaction (ORR).[26] The Shaik group recently published a computational study[27] characterizing two Fe/porphyrin complexes that contain cationic pyridinium residues in the secondary coordination sphere. Groves, in his original report on these complexes, showed that they undergo unprecedentedly fast C–H activation kinetics (Fig. 1d for the Fe^{III}–OH complex).[28,29] Shaik's study was able to reproduce activation energies from the experimental data through replacement of the charged functional groups with external oriented electrostatic fields, thereby implicating the catalytic effect as being almost purely electrostatic in origin.[27]

Beyond the electrostatic effects proposed by Tolman, Yang Savéant, and Groves/Shaik, little is known about the origin, magnitude, and impact of internal electrostatic fields on transition metal centers. Herein, we report a series of Cu^I complexes bound by novel tetradentate, tren-based tris(phosphinimine) ligands that exhibit a dramatic effect on the Cu^I/Cu^{II} redox potential. The major resonance contributors of the phosphinimine moieties of the ligands are the charge-separated, zwitterionic forms, in which a substantial amount of cationic charge on phosphorous results in the development of a cationic electrostatic field near an open coordination site at the metal center. The use of classical coordination chemistry, electrochemistry, and a textbook Jahn–Teller distortion allowed for an in-depth view into the effects brought by the development of strong, local electrostatic fields within this series of molecules.

Results and discussion

Ligand design and syntheses

Phosphinimines are often employed as strong, neutral, organic bases. Some are commercially available, and their pK_a values can range from 26 to 50, allowing for a multitude of applications.[30,31] These high basicities are on par with, or stronger than, the neutral bases 1,8-diazabicyclo(5.4.0)undec-7-ene (DBU), 1,1,3,3-tetramethylguanidine (TMG), and triazabicyclodecene (TBD),[32] and can be attributed to significant anionic character at the nitrogen atoms. Dyson and coworkers used DFT calculations to support the presence of significant ylidic character at the N–P bond of $HN=PH_3$ ($\delta_N = -1.28$; $\delta_P = +1.14$).[33] We calculated similar charge distributions for a series of *P*-substituted *N*-methyl phosphinimines, with the most notable
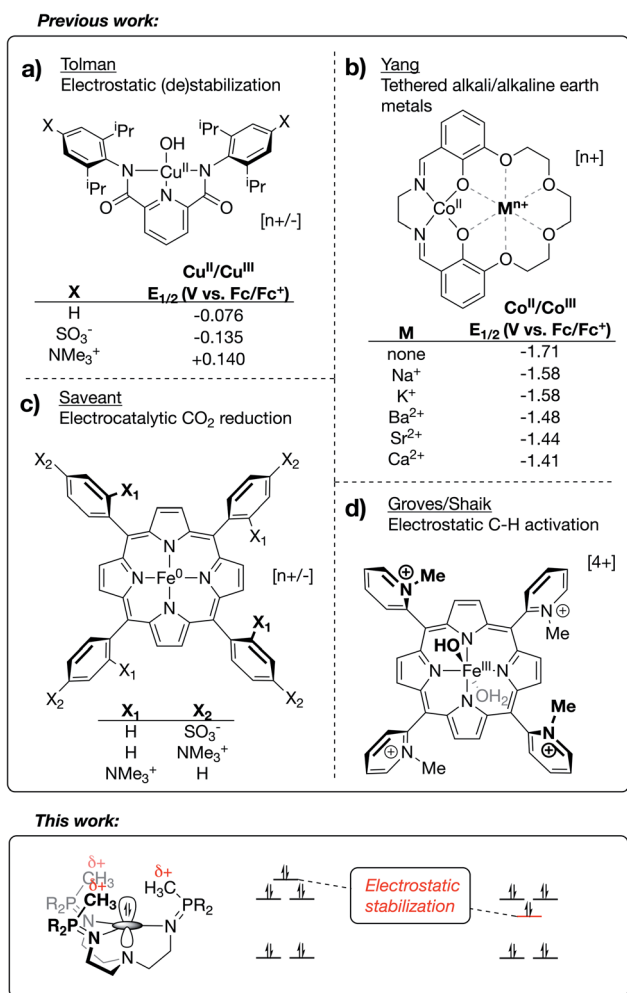

Fig. 1 Reported homogeneous inorganic complexes containing internal electrostatic fields generated *via* the incorporation of charged functional groups (a, c and d) or tethered redox-innocent metals (b) into the secondary coordination sphere.
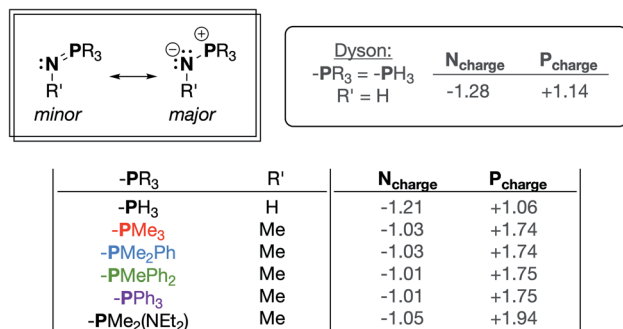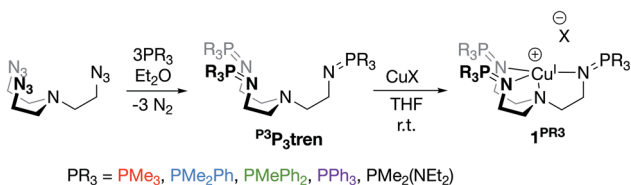
Fig. 2 Important resonance structures and select partial charges of truncated phosphinimine ligands as determined by natural population analyses (NPA). These charges are consistent with those calculated by Dyson and coworkers.[33]

change from the parent phosphinimine being an increase in the partial positive charge on phosphorus (δ_P) as alkyl/aryl/amido groups are introduced on phosphorus (Fig. 2).

We next sought to incorporate phosphinimine moieties into a multidentate ligand scaffold[34–41] with the intention of positioning multiple cationic phosphonium residues about a single open coordination site at a metal center. Ideally, the ligand would simultaneously take advantage of the strong σ-donation offered by the Lewis basic phosphinimine nitrogens.[42–47] A tris(2-aminoethyl)amine (tren) ligand backbone was selected due to the multitude of complexes bound by related ligands that have been described in the literature. The novel series of tren-based tris(phosphinimine)ligands ($^{R3}P_3$tren) were synthesized *via* the Staudinger reaction (Scheme 1), wherein the ratio of aryl:alkyl substituents bound to the phosphorous atoms in the secondary coordination sphere was systematically modulated (PR_3 = PMe_3, PMe_2Ph, $PMePh_2$, PPh_3). Additionally, in order to probe the impact of incorporating a strong electron-donating group bound to phosphorous, a PR_3 = $PMe_2(NEt_2)$ substituted ligand was synthesized following the same reaction scheme. These ligands were characterized using standard analytical techniques (see ESI†). The $^{31}P\{^1H\}$ NMR spectral resonances were identified at *ca.* 3 ppm, with a modest upfield shift as the number of aryl groups bound to phosphorous was increased. Notably, the $^{31}P\{^1H\}$ NMR spectral resonance for the PR_3 = $PMe_2(NEt_2)$ derivative was observed significantly downfield of the rest (20.79 ppm), indicative of a more electron-deficient phosphorous atom. This is consistent with the calculated δ_P values, which showed a marked increase for the $PMe_2(NEt_2)$-substituted phosphinimine compared to the all-alkyl/aryl-substituted analogs.

Synthesis of [$^{R3}P_3$tren-Cu]$^+$ complexes (1^{PR3}) and electrochemical studies

Treatment of $^{R3}P_3$tren with 1 equiv. of CuBAr$^F_4$·4MeCN (BAr$^F_4$ = B(C$_6$F$_5$)$_4^-$) in tetrahydrofuran (THF) afforded the cuprous complexes 1^{PR3} as white (1^{PMe3}) or yellow (1^{PMe2Ph}, 1^{PMePh2}, 1^{PPh3}, 1$^{PMe2(NEt2)}$) solids (Scheme 1). Crystallographic analyses of 1^{PMe3}, 1^{PMe2Ph}, and 1^{PPh3} revealed trigonal pyramidal complexes (Fig. 3). The Cu–N$_{ax}$ distances range from 2.175–2.236 Å (1^{PMe2Ph} < 1^{PMe3} < 1^{PPh3}), and the Cu–N$_{eq}$ distances range from 2.017–2.081 Å (1^{PMe3} < 1^{PPh3} < 1^{PMe2Ph}). Neither trend was found to correlate with the steric bulk of the phosphorus substituents. Notably, the vacant axial coordination site of 1^{PMe3} is retained in the solid state, irrespective of the identity of the anion or the presence of Lewis basic solvents (see ESI†). NMR spectra of 1^{PR3} were obtained in CD$_3$CN and found to display C_{3v} symmetry on the NMR timescale; single $^{31}P\{^1H\}$ resonances were located downfield (between 20 and 25 ppm) of those for the free ligands ($^{R3}P_3$tren). For 1$^{PMe2(NEt2)}$, the single spectral resonance corresponding to the phosphorous environment is observed further downfield at 38.11 ppm.

Electrochemical studies of 1^{PR3} were undertaken in iso-butyronitrile (IBN) and are reported relative to Fc/Fc$^+$. As shown in Fig. 4, 1^{PR3} displayed quasi-reversible $E_{1/2}$ features that we assign as the Cu^I/Cu^{II} redox couples. The most anodic feature was observed for 1^{PPh3} at −415 mV. As the ratio of alkyl:aryl substituents bound to phosphorous increased, a cathodic shift in the Cu^I/Cu^{II} redox potential was observed, culminating with 1^{PMe3} at −780 mV. This $E_{1/2}$ value is remarkably reducing, and to the best of our knowledge represents the most cathodic Cu^I/Cu^{II} redox couple for this geometry reported to date. The trend in redox potentials suggested that an increase in the number of alkyl groups on phosphorus caused an increase in the σ-donation of the phosphinimine nitrogen to Cu, thereby creating increasingly electron-rich metal centers across the series.
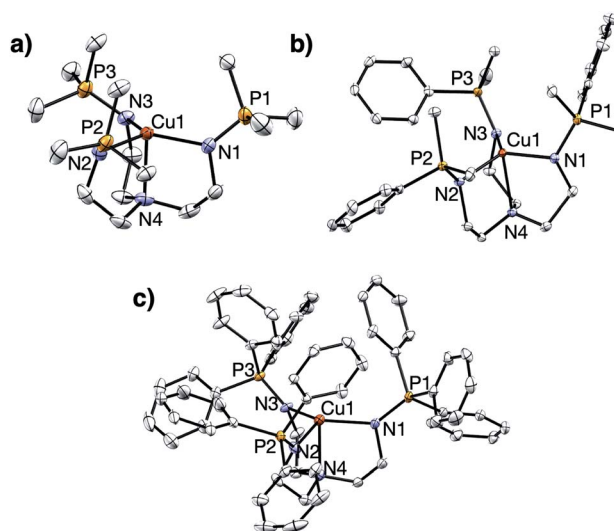

Fig. 3 Solid state structures of (a) 1^{PMe3}, (b) 1^{PMe2Ph}, and (c) 1^{PPh3}. Ellipsoids shown at 50% probability; hydrogen atoms and anions omitted for clarity.

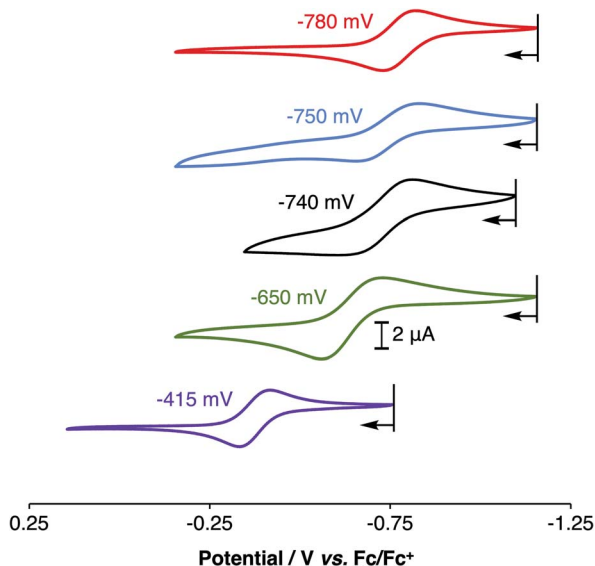Scheme 1 Syntheses of $^{R3}P_3$tren ligands and their Cu^I complexes.

PR_3 = PMe_3, PMe_2Ph, $PMePh_2$, PPh_3, $PMe_2(NEt_2)$

Fig. 4 Cyclic voltammograms of 1^{PMe3} (red), 1^{PMe2Ph} (blue), $1^{PMe2(NEt2)}$ (black), 1^{PMePh2} (green), and 1^{PPh3} (purple), showing their Cu^I/Cu^{II} redox couples in isobutyronitrile (IBN).

However, $1^{PMe2(NEt2)}$, which would be expected to have the strongest σ-donation due to the increased anionic character on the nitrogen donor atom, was found to have a Cu^I/Cu^{II} couple of −740 mV, a value that is 40 mV more anodic than the Cu^I/Cu^{II} redox couple of 1^{PMe3} and similar to the redox couple observed for 1^{PMe2Ph}. Combined with the structural data, these results indicate that the secondary coordination sphere plays a role in the electronic structures of the metal centers across this series. We thus turned to density functional theory (DFT) to generate an impression of the valence manifold that could be carried into further experimental studies with this system.

DFT calculations on 1^{PR3} and comparison to literature analogs

DFT calculations on 1^{PR3} were compared to a series of literature examples selected for the similarities they offer in terms of structure and donor type (Fig. 5a). The most facile point of comparison is tren-Cu^I, which shares the architecture and N_4 donor set of P_3tren. We have similarly included the TMG_3tren-Cu^I complex due to parallels between the basic guanidyl groups of this ligand and the phosphinimine groups on 1^{PR3}. Other recent ligand design efforts have generated Cu^I centers in similar geometries but with widely varying redox potentials. Karlin and coworkers reported a series of ^{X}TMPA-Cu^I complexes (TMPA = tris(2-pyridylmethyl)amine) wherein a systematic change in the Cu^I/Cu^{II} redox couple was attained through substitution at the para-positions of the TMPA pyridyl rings.[48] Introducing electron-donating groups at these positions resulted in a shift of the Cu^I/Cu^{II} couple to more negative potentials, ultimately attaining a potential of −0.70 V (vs. Fc/Fc⁺) for the dimethylamino-substituted ^{X}TMPA derivative (^{NMe2}TMPA). This value was ~0.3 V more cathodic than the Cu^I complex bound by the parent ligand (^{H}TMPA).
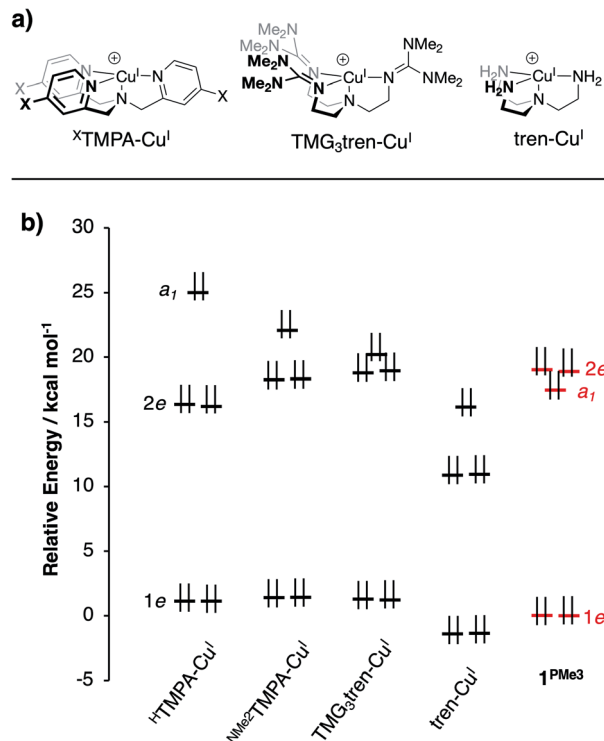

Fig. 5 (a) Cu^I complexes from the literature for computational comparison to 1^{PR3}, and (b) DFT-calculated MO diagram for Cu^I complexes (energies referenced arbitrarily to $1e$ of 1^{PMe3}).

DFT geometry optimizations were performed on the cations of 1^{PR3}, tren-Cu^I, TMG_3tren-Cu^I, ^{H}TMPA-Cu^I, ^{tBu}TMPA-Cu^I, ^{OMe}TMPA-Cu^I, and ^{NMe2}TMPA-Cu^I. In accord with available experimental data, it was found that MeCN coordination to ^{H}TMPA-Cu^I was energetically favorable, forming a 20 e⁻ complex. The other Cu^I complexes preferentially retained an open coordination site trans to the tertiary nitrogen. The geometries for all four-coordinate complexes were best described as trigonal pyramidal, and the five-coordinate MeCN adduct of ^{H}TMPA-Cu^I adopted a C_{3v} geometry that is best described as trigonal bipyramidal. In all cases, the calculated bond distances about copper provided excellent agreement with experimental data (see ESI†). One observation that will be important to the ensuing discussion is that the trend in $Cu–N_{ax}$ distances observed experimentally ($1^{PMe2Ph} < 1^{PMe3} < 1^{PPh3}$) was reproduced using these computational methods.

The calculations revealed an interesting trend in the ligand field splitting pattern. The pseudo-C_{3v}-symmetric geometries allow for valence manifolds containing nearly degenerate e-sets of d_{xz}/d_{yz} character ($1e$) and $d_{x^2-y^2}/d_{xy}$ character ($2e$), along with an a_1-symmetric d_{z^2} orbital. For ^{H}TMPA-Cu^I-MeCN, ^{tBu}TMPA-Cu^I, ^{OMe}TMPA-Cu^I, ^{NMe2}TMPA-Cu^I, TMG_3tren-Cu^I, and tren-Cu^I, $1e$ is lowest in energy, followed by $2e$, and then a_1 as the HOMO, creating 2 : 2 : 1 d-manifold splitting pattern. As expected, ^{H}TMPA-Cu^I–MeCN exhibits the highest energy a_1 due to the ligand field effect of the additional axial donor. Removal of MeCN leads to the trigonal pyramidal ^{H}TMPA-Cu^I model compound suitable for comparison to the other four-coordinate

complexes in this series (Fig. 5b); this four-coordinate species retains the 2 : 2 : 1 splitting pattern of the other ^{X}TMPA congeners.

For $\mathbf{1^{PR3}}$, the d-manifolds switch to 2 : 1 : 2 configurations, with the $2e$ set containing the HOMO and HOMO−1 (Fig. 5b for $\mathbf{1^{PMe3}}$). This inversion in the valence manifold splitting pattern may be thought to result from two primary contributors. First, the stronger ligand field strength of the partially anionic phosphinimine nitrogen σ-donors creates a larger split between $1e$ and $2e$, effectively raising the energy of $2e$ in $\mathbf{1^{PR3}}$ relative to $2e$ in the reference compounds. Second, a significant variation in the relative energy of a_1 (d$_{z^2}$) was observed. The energy of a_1 decreases from TMPA-Cu^I to ^{tBu}TMPA-Cu^I, ^{OMe}TMPA-Cu^I, ^{NMe2}TMPA-Cu^I, TMG$_3$tren-Cu^I, and tren-Cu^I. As expected, this trend was found to correlate closely with the Cu–N$_{ax}$ bond distance, as the ligand field strength in the axial direction will exert the most influence on the destabilization of d$_{z^2}$ ($R^2 = 0.98$; Fig. 6, yellow); *i.e.* the longer the Cu–N$_{ax}$ distance, the lower the a_1 energy. The $\mathbf{1^{PR3}}$ complexes, however, provide notable deviations from this trend. Using $\mathbf{1^{PMe3}}$ as an example, the predicted Cu–N$_{ax}$ distance of 2.244 Å would be expected to result in an a_1 energy of *ca.* 23.3 kcal mol^{-1}, but the energy of a_1 is instead calculated to lie nearly 6 kcal mol^{-1} lower in energy (17.5 kcal mol^{-1}, Fig. 6, red). This unexpected and significant decrease in the energy of a_1 appears to work in concert with the aforementioned destabilization of $2e$ to create the 2 : 1 : 2 ligand field splitting pattern. Similar effects for $\mathbf{1^{PMe2Ph}}$, $\mathbf{1^{PMe2(NEt2)}}$, and $\mathbf{1^{PMe2Ph}}$ are observed, to varying degrees (Fig. 6, blue, black, and green).

On considering the ylidic character of the phosphinimines and the geometric constraints imposed by the tren backbone of the ^{R3}P$_3$tren ligands, the possibility arose that the deviations in the energy of a_1 may reflect stabilization from cationic electrostatic fields emanating from the phosphonium residues. This view is supported by evaluation of the electrostatic potential along the canonical z-axis radiating away from the copper centers in the complexes evaluated above. In the absence of electrostatic fields in the secondary coordination sphere, one would expect the potential experienced by a test charge placed along this vector to diminish with a *ca.* $1/r$ dependence, according to the coulombic interaction of that test charge with the Cu ion. Indeed, this behavior is observed for ^{H}TMPA-Cu^I, ^{tBu}TMPA-Cu^I, ^{OMe}TMPA-Cu^I, ^{NMe2}TMPA-Cu^I, and tren-Cu^I (Fig. 7). However, deviations from $1/r$ behavior of the electrostatic potential are apparent in the cases of $\mathbf{1^{PR3}}$ (Fig. 7). In these cases, clear maxima along the z-axis are observed at *ca.* 2.75 Å, a position that lies in-plane with the three nearest phosphonium carbon atoms, which are *ca.* 2.5 Å from the z-axes. Evaluation of the electrostatic potential gradients along the z-axes for $\mathbf{1^{PR3}}$ predicts the presence of local electrostatic fields, located at *ca.* 2.2 Å from the copper centers, ranging in magnitude from 3–12 V nm^{-1} (Fig. S1–S3†). These field strengths are on par with what has been measured both in enzymes using vibrational Stark spectroscopy[2–4] and in organized matter *via* neutron and synchrotron/X-ray diffraction studies,[5] and it would therefore be large enough in magnitude to interact with the electron pair in a_1. The TMG$_3$tren-Cu^I complex also shows a modest deviation from the expected $1/r$ dependence in electrostatic potential, rising at *ca.* 2 Å to a plateau in electrostatic potential that persists to *ca.* 4 Å from the copper center (Fig. 7). This may be thought to result from the contribution of ionic resonance pictures available to the guanidinyl units in which a cationic charge is located on one of the amino nitrogen atoms. The modest deviation in electrostatic potential in this case is consistent with the crystallographic data, which indicate that the TMG groups show minor contributions from these ionic resonance structures.

Deviations in the a_1 orbital energies (Fig. 6) increase in order from $\mathbf{1^{PMePh2}} < \mathbf{1^{PMe3}} < \mathbf{1^{PMe2Ph}} \approx \mathbf{1^{PMe2(NEt2)}}$. This ordering was found to directly correlate with the calculated strength of the electrostatic field present along the canonical z-axes of the molecules (Fig. 8, green triangles), thereby implicating the
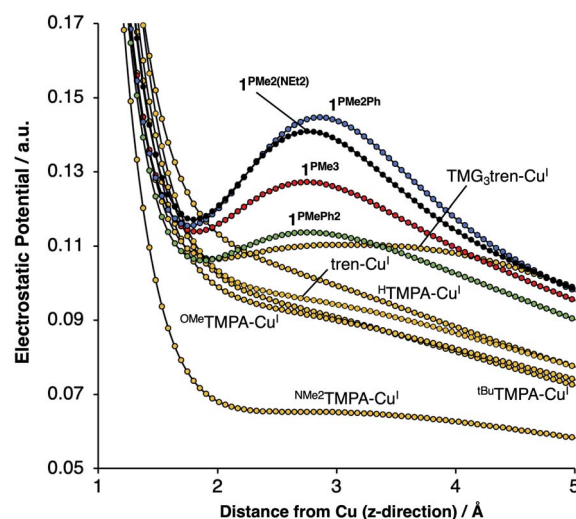

Fig. 6 Calculated energies of a_1 as a function of the calculated Cu–N$_{ax}$ bond distances ($R^2 = 0.98$).

Fig. 7 One-dimensional electrostatic potential map along the canonical z-axes of the Cu^I complexes.
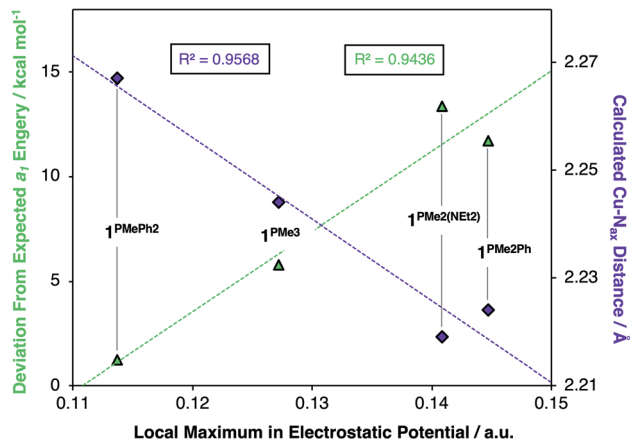
Fig. 8 Correlations between the ~2.75 Å local maxima in electrostatic potential and (i) a_1 orbital energies (green triangles, left y-axis, R^2 = 0.96) and (ii) calculated Cu−N$_{ax}$ bond lengths (purple diamonds, right y-axis, R^2 = 0.94).
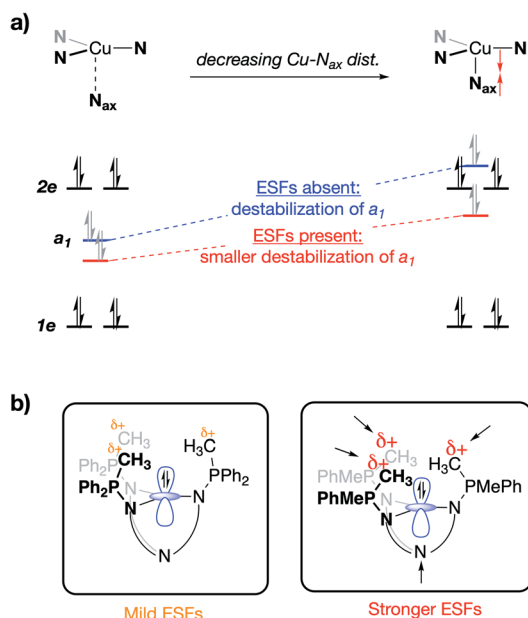

Fig. 9 (a) qualitative MO diagram showing the impact of the Cu−N$_{ax}$ distance on the a_1 orbital without stabilizing ESFs (blue), and with stabilizing ESFs (red), and (b) the stereoelectronic impact of an enhanced attraction between a_1 and the phosphonium residues as a function of the strength of the internal ESFs.

cationic phosphonium residues as having a through-space electrostatic stabilizing effect on a_1 (Fig. 9a). The strengths of the electrostatic fields in 1^{PR3} were also found to inversely correlate with the calculated Cu−N$_{ax}$ distances (Fig. 8, purple diamonds). This observation suggests that electrostatic attractions between the occupied a_1 orbitals and the phosphonium residues work in concert with the rigidity of the ligand backbones to pull the N$_{ax}$ atoms closer to the copper centers (Fig. 9b). This stereoelectronic effect is significant in that it represents a physical consequence of electrostatic stabilization of a_1. Together, the observations discussed within this section

support a direct relationship between the physical properties observed in this system and the magnitude of the electrostatic fields emanating from the cationic phosphonium residues in the secondary coordination spheres in 1^{PR3}.

Chemical oxidation of 1^{PMe3} and DFT analysis of the Cu^{II} products

To validate the computationally predicted valence manifolds for 1^{PR3}, we performed chemical oxidations of one of the P$_3$tren-Cu^I complexes. The 2 : 1 : 2 d-orbital splitting patterns calculated for 1^{PR3} suggest that 1 e$^-$ oxidations would generate holes with significant 2e character. The resulting Cu^{II} complexes would contain doubly degenerate electronic ground states, which would then be susceptible to primary Jahn–Teller distortions. By contrast, the 2 : 2 : 1 d-orbital splitting pattern predicted for the other compounds in this class would yield singly degenerate S = 1/2 states upon oxidation, precluding Jahn–Teller distortions from occurring. Thus, the presence or absence of a Jahn–Teller distortion in the Cu^{II} analog of 1^{PMe3} may be used to resolve the structure of the Cu^I valence manifold.

Upon treatment of 1^{PMe3} with AgBAr$^F_4$·4MeCN in THF, the colorless solution immediately turned red, concomitant with precipitation of a dark solid (Ag^0). The Cu^{II} product proved resistant to crystallization, but independent synthesis of the dication through ligation of cupric triflate with ^{Me3}P$_3$tren in MeCN afforded [(^{Me3}P$_3$tren)Cu][OTf]$_2$ (2^{PMe3}, Fig. 10a). This red material shows the same UV-vis spectral features as the oxidation product described above and the same cyclic voltammetry trace as 1^{PMe3} (Fig. S15†). Single crystals of 2^{PMe3} were grown by diffusion of pentane into a 1,2-difluorobenzene (DFB) solution of the complex; however, radiative decay of the crystalline sample during X-ray diffraction experiments (Cu-Kα radiation source, λ = 1.5406 Å) resulted in incomplete data set collection and subsequently poor X-ray model refinement (R = 27%). Although the exact bond lengths and angles derived from the preliminary solid-state structure of 2^{PMe3} are not statistically reliable, the data were adequate to reveal a four-coordinate Cu^{II} complex clearly distorted to a pseudo-C_s symmetry via a Jahn–Teller distortion (Fig. 10b).

This result may be contrasted with the 1-electron oxidation of 1^{PMe3} using triphenylmethyl chloride, which resulted in the formation of the yellow/green five-coordinate complex [(^{Me3}P$_3$-tren)CuCl][OTf] (3^{PMe3}, Fig. 10a), which exists in the solid-state as a pseudo-C_{3v}-symmetric complex with an axial chloride ligand. Significant differences in the solid-state geometries between 2^{PMe3} and 3^{PMe3} are highlighted in the selected bond distances and angles shown in Fig. 10b. Complex 2^{PMe3} exhibits shorter Cu−N$_{eq}$ distances, a longer Cu−N$_{ax}$ distance, and a marked distortion of the equatorial donors from a nearly trigonal geometry in 3^{PMe3} (<N$_{eq}$−Cu−N$_{eq}$ = 113°–126°) to a T-shaped geometry in 2^{PMe3} (<N$_{eq}$−Cu−N$_{eq}$ = 106°–147°).

DFT geometry optimization calculations on the cationic portion of 2^{PMe3} replicated the Jahn–Teller distortion observed experimentally, regardless of the starting geometry (Fig. 10c, left, β (spin down) orbitals). As expected, the distortion lifted the degeneracy of 2e, increasing the energy of the singly
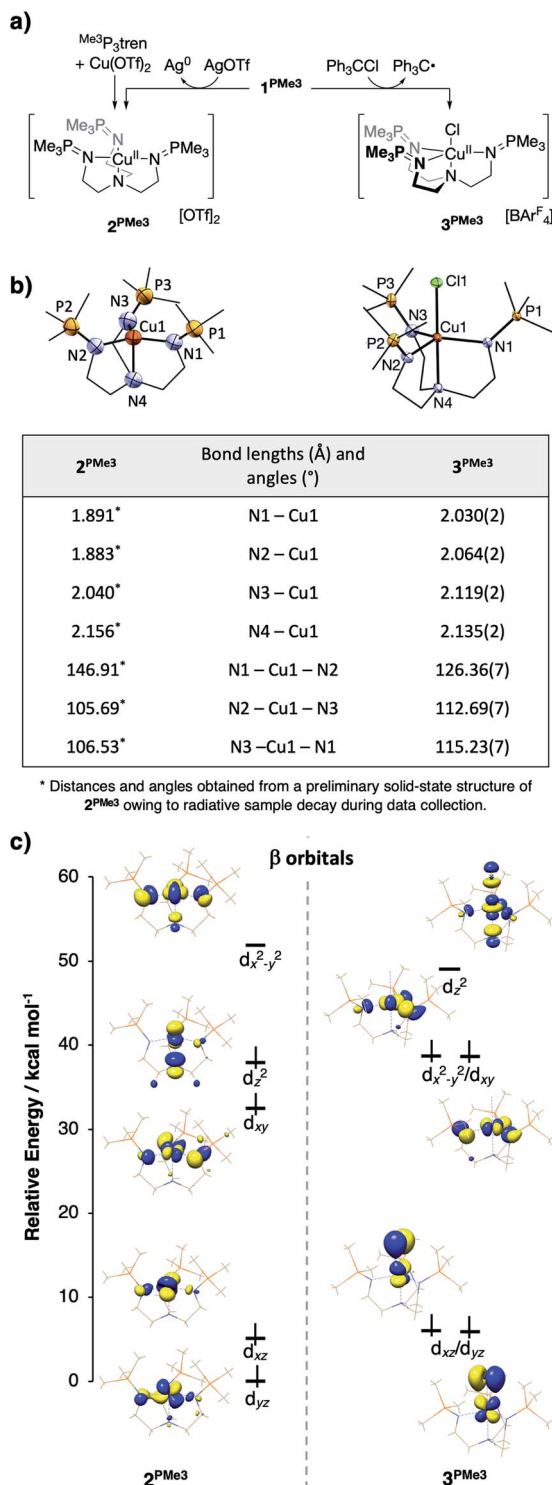
Fig. 10 (a) Synthetic schemes for 2^{PMe3} and 3^{PMe3}, (b) solid state structures of 2^{PMe3} and 3^{PMe3} with select bond distances and angles tabulated below (structural data for 2^{PMe3} are preliminary due to incomplete data set collection stemming from radiative sample degradation during the XRD experiment), and (c) DFT-derived molecular orbital diagrams showing the β (spin down) d-manifold for 2^{PMe3} and 3^{PMe3}.

occupied $d_{x^2-y^2}$ and decreasing the energy of d_{xy}. In an effort to examine the uniqueness of the Jahn–Teller distortion observed in 2^{PMe3}, the analogous, four-coordinate Cu^{II} complexes bound

by ^HTMPA, $^{tBu}TMPA-Cu^I$, $^{OMe}TMPA-Cu^I$, $^{NMe2}TMPA$, TMG_3tren, and tren were evaluated by the same methods as those used for 2^{PMe3}. The calculated Cu^{II} ions were found to exhibit C_{3v} symmetry, closely matching the experimental geometries, and consistent with the presence of an a_1-symmetric vacancy. Comparable DFT analysis of the five-coordinate complex 3^{PMe3} supports the conclusion that its 3-fold symmetry results from Cl^- destabilization of d_{z^2}, thereby reverting the ligand field splitting to a 2 : 2 : 1 pattern (Fig. 10c, right, β orbitals) that is inactive toward a Jahn–Teller distortion for a d^9 metal ion.

Time-dependent density functional theory (TD-DFT) predictions added support that the valence manifold structures of the red Cu^{II} species 2^{PMe3} and the green Cu^{II} species 3^{PMe3} both persist in the solution phase. The experimentally measured UV-
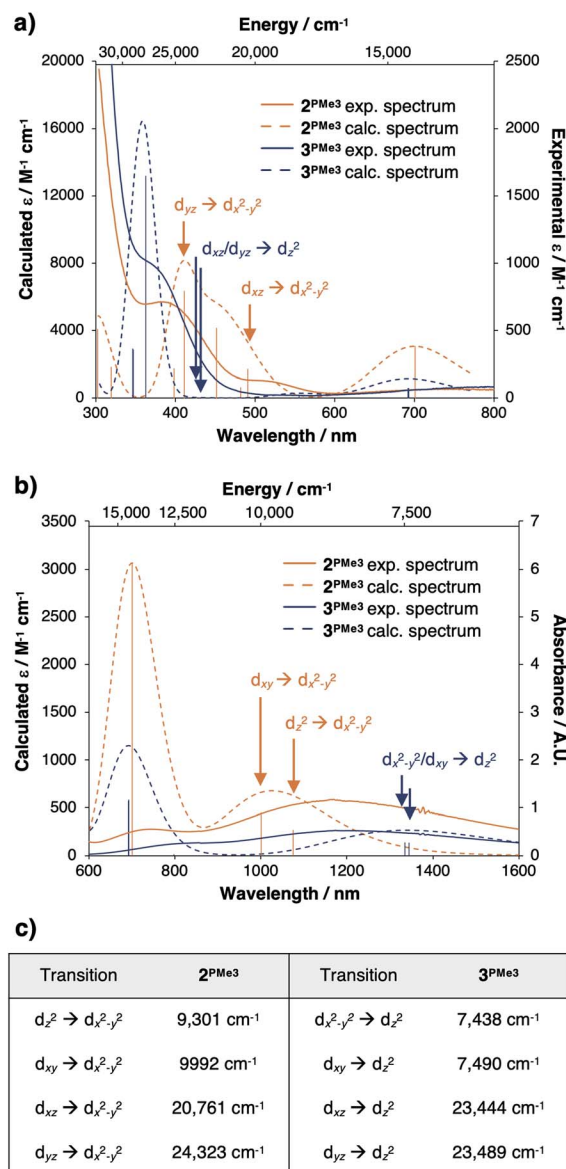

Fig. 11 (a) Experimental and TD-DFT generated UV-vis spectra of 2^{PMe3} and 3^{PMe3}, (b) near-IR region of the electronic spectra for 2^{PMe3} and 3^{PMe3}, and (c) tabulated d−d transitions for 2^{PMe3} and 3^{PMe3}. Calculated d−d transitions are indicated on the spectra with arrows.

vis spectrum of 2^{PMe3} (Fig. 11a and b, solid orange trace) contains three prominent features at *ca.* 400 nm (25 000 cm^{-1}), 526 nm (19 000 cm^{-1}), and 700 nm (14 200 cm^{-1}) that were reproduced computationally (Fig. 11a and b, dashed orange trace). The feature at 400 nm is assigned as the $d_{yz} \rightarrow d_{x^2-y^2}$ transition, and the feature at 526 nm is assigned as the $d_{xz} \rightarrow d_{x^2-y^2}$ transition. The feature calculated at 700 nm is best described as a ligand to metal charge transfer (LMCT) from the phosphinimine moieties to the empty $d_{x^2-y^2}$ β orbital, though the experimental and calculated intensities are both predicted to be low. A single broad feature is observed in the near infrared spectrum (NIR) (Fig. 11b, solid orange trace) at *ca.* 1190 nm (8403 cm^{-1}) that was reproduced computationally (Fig. 11b, dashed orange trace) as a combination of the $d_{xy} \rightarrow d_{x^2-y^2}$ and $d_{z^2} \rightarrow d_{x^2-y^2}$ transitions.

The experimental UV-vis spectrum of 3^{PMe3} (Fig. 11a, solid blue trace) contains prominent features at *ca.* 360 nm (27 800 cm^{-1}) and 750 nm (13 300 cm^{-1}), which were also reproduced computationally (27 800 cm^{-1} and 14 388 cm^{-1}) (Fig. 11a, dashed blue trace). Although the $d_{xz}/d_{yz} \rightarrow d_{z^2}$ transitions are predicted to be within this energy range (23 444, 23 489 cm^{-1}), they are likely not observed due to low intensities (ε_{calc} = 13–14 M^{-1} cm^{-1}). A single broad feature is observed in the NIR spectrum of 3^{PMe3} (Fig. 11b, solid blue trace) that was reproduced computationally (Fig. 11b, dashed blue trace) as the $d_{xy}/d_{x^2-y^2} \rightarrow d_{z^2}$ transitions. The calculated energies of the various d–d transitions for 2^{PMe3} and 3^{PMe3} are tabulated in Fig. 11c and are marked on the spectra in Fig. 11a and b with arrows (orange for 2^{PMe3}, blue for 3^{PMe3}).

DFT evaluation of the Cu^I/Cu^{II} redox potentials

The calculated redox potentials for this series of complexes were evaluated as a way to gauge the extent to which the Jahn–Teller distortions, the phosphinimine donor strengths, and the through space electrostatic effects individually contribute to the highly cathodic Cu^I/Cu^{II} couples. As mentioned above, Karlin and co-workers have shown that variations in the donor strength of TMPA-based ligands significantly impacts Cu^I/Cu^{II} redox potentials, and the Tolman group has used distal charged residues to influence Cu^{II}/Cu^{III} redox potentials as a function of the sign of the charged group. Jahn–Teller effects have also been shown to impact the thermodynamics of electron transfer. For example, a ∼0.6 V shift in redox potentials for a series of Cu^I bis(1,10-phenanthroline) complexes has been ascribed to the varying extent of Jahn–Teller distortion available to the complexes as a function of the steric bulk in their secondary coordination spheres.[49–51]

In the present case, the trends in the experimental redox potentials were reproduced computationally for 1^{PMe3} and the ^{X}TMPA-Cu^I complexes[48] discussed above (Table 1). The mean unsigned error of 120 mV is on par with the current state-of-the-art.[52] In order to evaluate the impact of the Jahn–Teller distortion in 2^{PMe3} on the Cu^I/Cu^{II} redox potential, a C_{3v}-symmetric analog of 2^{PMe3} was evaluated by constraining the N$_{eq}$–Cu–N$_{eq}$ angles to 120°. The structure optimized with this constraint was then used to calculate a hypothetical Cu^I/Cu^{II} redox potential in

Table 1 Calculated and experimental Cu^I/Cu^{II} redox couples for complexes with available experimental data.[42] The error represents the signed error between experiment and calculation. Average unsigned error = 120 mV

Complex	Calc. pot. (mV)	Exp. pot. (mV)	Error (mV)
1^{PMe3} (C_{3v}-Cu^I/C_s-Cu^{II})	−890	−780	−110
1^{PMe3} (C_{3v}-Cu^I/C_{3v}-Cu^{II})	−630		+150
1^{PMe2Ph}	−579	−750	+171
$1^{PMe2(NEt2)}$	−822	−740	−82
1^{PMePh2}	−640	−650	+10
^{H}TMPA-Cu^I	−232	−400	+168
^{tBu}TMPA-Cu^I	−303	−460	+157
^{OMe}TMPA-Cu^I	−311	−490	+179
^{NMe2}TMPA-Cu^I	−617	−700	+83

which the Cu^I symmetry is maintained upon oxidation of 1^{PMe3} (denoted as C_{3v}-Cu^I/C_{3v}-Cu^{II}). This redox couple (−630 mV) is on par with the calculated redox potential for ^{NMe2}TMPA-Cu^I (−617 mV), indicating that the phosphinimine donors act as strong σ-donors to create electron-rich Cu^I centers. Importantly, however, the C_{3v}-Cu^I/C_{3v}-Cu^{II} potential is calculated to be substantially more anodic than the Cu^I/Cu^{II} redox potential that takes into account the Jahn–Teller distortion on oxidation (C_{3v}-Cu^I/C_s-Cu^{II}, −890 mV; Table 1). This 260 mV shift in potential indicates that the geometric change accompanying oxidation provides a substantial driving force (*ca.* 6 kcal mol^{-1}) for electron transfer from 1^{PMe3}.

It remained to consider the origin of the >350 mV range in redox potentials for 1^{PR3}. The potentials do not clearly track with the donor strengths of the phosphinimines, and the characterization of the oxidation as being 2e ($d_{x^2-y^2}/d_{xy}$)-based suggests that the extent of electrostatic stabilization of a_1 is not responsible. This is supported by the observation that the magnitude of the electrostatic potential along the canonical z-axis does not scale with the Cu^I/Cu^{II} redox couple. We thus hypothesized that the steric bulk of the phosphinimine substitutions was responsible for modulating the extent to which the Jahn–Teller distortion stabilized the oxidized Cu^{II} ions.

This steric effect was evaluated through calculation of a modified Tolman cone angle (θ^*) for the phosphinimine substituents in the ^{R3}P$_3$tren ligands (see ESI† for details on the calculation of θ^*). Upon plotting the experimental Cu^I/Cu^{II} redox potentials *versus* θ^*, a direct relationship between steric bulk in the secondary coordination sphere and the Cu^I/Cu^{II} redox potential is realized (Fig. 12). Indeed, for cone angles >140°, a linear relationship (R^2 = 0.99) is observed. This observation can be explained by considering that the maximum amount of stabilization of the Cu^{II} species (and thus the most cathodic Cu^I/Cu^{II} redox potential) will occur for ligands with small values of θ^*, for which the limited steric profile of the ligand allows for the most distortion by the tethered arms of the ligand backbone. As the steric profile of the ligand increases, the Cu^{II} species become increasingly prohibited from accessing
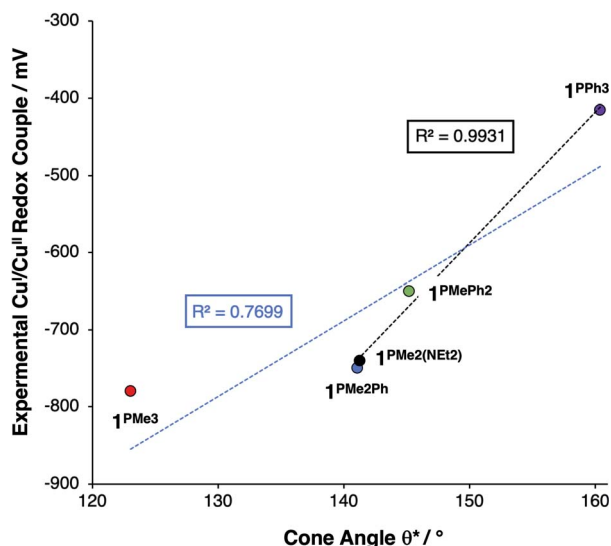
Fig. 12 Plot of redox potential *versus* θ^*, showing a linear relationship between potential and the steric bulk of the ligand for values of $\theta^* \geq 141°$ (black trendline, $R^2 = 0.99$). The blue trendline ($R^2 = 0.77$) includes all five data points.
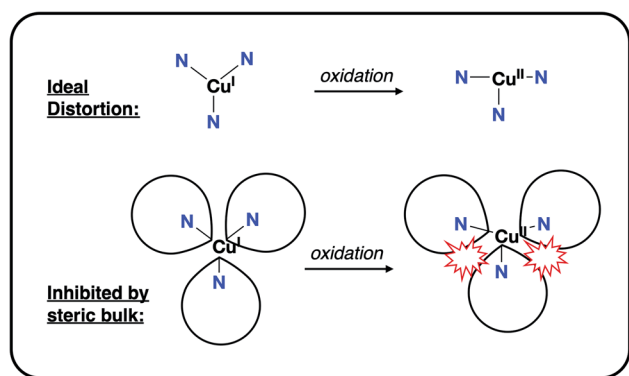

Fig. 13 Depiction of the inhibition of an "ideal" Jahn–Teller distortion with increased steric bulk in the secondary coordination sphere.

Jahn–Teller-distorted geometries (Fig. 13), resulting in a systematic anodic shift in the Cu^I/Cu^{II} redox potentials. The non-linearity of the data shown in Fig. 12 on inclusion of 1^{PMe3} suggests that a lower bound for the cone angle at which the Jahn–Teller distortion is inhibited lies between $123°$ and $141°$. Overall, these data indicate that while electrostatic effects appear to be critical for engendering a Jahn–Teller distortion in 2^{PR3}, the steric profile of the secondary coordination sphere is responsible for fine-tuning the Cu^I/Cu^{II} redox potentials.

Conclusions

This study demonstrates the ability of strategically-placed charged residues to directly impact the valence manifolds of homogeneous inorganic complexes. This technique is independent of the specific donor bound to the metal center,

allowing for orthogonal control of valence orbital energies by way of through-bond and through-space effects. In the present example, electrostatic fields (ESFs) emanating from cationic phosphonium residues in the secondary coordination spheres of 1^{PR3} stabilize the valence MO a_1 (d_{z^2}) orbitals. This stabilization would typically result in an anodic shift in redox potential, but the strong σ-donation from the phosphinimine donors provides an orthogonal destabilization of the Cu^I $2e$ set, producing counter-intuitive shifts in Cu^I/Cu^{II} redox potentials. The resulting inversion of the valence manifold brought by these complementary effects generates a system capable of undergoing a Jahn–Teller distortion upon oxidation, providing an additional thermodynamic driving force for electron transfer. Studies to assess the impact of ESFs on small molecule binding and reactivity are underway.

Conflicts of interest

There are no conflicts to declare.

Acknowledgements

References

1 A. Warshel, P. K. Sharma, M. Kato, Y. Xiang, H. Liu and M. H. M. Olsson, *Chem. Rev.*, 2006, **106**, 3210–3235.

2 S. D. Fried, S. Bagchi and S. G. Boxer, *Science*, 2014, **346**, 1510–1514.

3 M. G. Romei, C.-Y. Lin, I. I. Mathews and S. G. Boxer, *Science*, 2020, **367**, 76–79.

4 S. D. Fried and S. G. Boxer, *Annu. Rev. Biochem.*, 2017, **86**, 387–415.

5 M. W. Shi, S. P. Thomas, V. R. Hathwar, A. J. Edwards, R. O. Piltz, D. Jayatilaka, G. A. Koutsantonis, J. Overgaard, E. Nishibori, B. B. Iversen and M. A. Spackman, *J. Am. Chem. Soc.*, 2019, **141**, 3965–3976.

6 C. F. Gorin, E. S. Beh, Q. M. Bui, G. R. Dick and M. W. Kanan, *J. Am. Chem. Soc.*, 2013, **135**, 11257–11265.

7 C. F. Gorin, E. S. Beh and M. W. Kanan, *J. Am. Chem. Soc.*, 2012, **134**, 186–189.

8 A. C. Aragonès, N. L. Haworth, N. Darwish, S. Ciampi, N. J. Bloomfield, G. G. Wallace, I. Diez-Perez and M. L. Coote, *Nature*, 2016, **531**, 88–91.

9 V. M. Lau, W. C. Pfalzgraff, T. E. Markland and M. W. Kanan, *J. Am. Chem. Soc.*, 2017, **139**, 4035–4041.

10 M. Klinska, L. M. Smith, G. Gryn'ova, M. G. Banwell and M. L. Coote, *Chem. Sci.*, 2015, **6**, 5623–5627.

11 G. Gryn'ova and M. L. Coote, *Aust. J. Chem.*, 2017, **70**, 367–372.

12 K. Zhang, B. B. Noble, A. C. Mater, M. J. Monteiro, M. L. Coote and Z. Jia, *Phys. Chem. Chem. Phys.*, 2018, **20**, 2606–2614.

13 L. Zhang, E. Laborda, N. Darwish, B. B. Noble, J. H. Tyrell, S. Pluczyk, A. P. Le Brun, G. G. Wallace, J. Gonzalez, M. L. Coote and S. Ciampi, *J. Am. Chem. Soc.*, 2018, **140**, 766–774.

14 L. Zhang, Y. B. Vogel, B. B. Noble, V. R. Gonçales, N. Darwish, A. Le Brun, J. J. Gooding, G. G. Wallace, M. L. Coote and S. Ciampi, *J. Am. Chem. Soc.*, 2016, **138**, 9611–9619.

15 M. T. Blyth, B. B. Noble, I. C. Russell and M. L. Coote, *J. Am. Chem. Soc.*, 2020, **142**, 606–613.

16 N. S. Hill and M. L. Coote, *Aust. J. Chem.*, 2019, **72**, 627–632.

17 M. T. Blyth and M. L. Coote, *J. Org. Chem.*, 2019, **84**, 1517–1522.

18 L.-J. Yu and M. L. Coote, *J. Phys. Chem. A*, 2019, **123**, 582–589.

19 N. S. Hill and M. L. Coote, *J. Am. Chem. Soc.*, 2018, **140**, 17800–17804.

20 H. M. Aitken and M. L. Coote, *Phys. Chem. Chem. Phys.*, 2018, **20**, 10671–10676.

21 D. Dhar, G. M. Yee and W. B. Tolman, *Inorg. Chem.*, 2018, **57**, 9794–9806.

22 A. H. Reath, J. W. Ziller, C. Tsay, A. J. Ryan and J. Y. Yang, *Inorg. Chem.*, 2017, **56**, 3713–3718.

23 T. Chantarojsiri, J. W. Ziller and J. Y. Yang, *Chem. Sci.*, 2018, **9**, 2567–2574.

24 T. Chantarojsiri, A. H. Reath and J. Y. Yang, *Angew. Chem., Int. Ed.*, 2018, **57**, 14037–14042.

25 I. Azcarate, C. Costentin, M. Robert and J.-M. Savéant, *J. Am. Chem. Soc.*, 2016, **138**, 16639–16644.

26 D. J. Martin, B. Q. Mercado and J. M. Mayer, *Sci. Adv.*, 2020, **6**, eaaz3318.

27 T. Stuyver, R. Ramanan, D. Mallick and S. Shaik, *Angew. Chem., Int. Ed.*, 2020, **59**, 7915–7920.

28 H. Gao and J. T. Groves, *J. Am. Chem. Soc.*, 2017, **139**, 3938–3941.

29 S. R. Bell and J. T. Groves, *J. Am. Chem. Soc.*, 2009, **131**, 9640–9641.

30 J. Verkade, *Angew. Chem., Int. Ed.*, 2009, **48**, 9221.

31 I. Kaljurand, J. Saame, T. Rodima, I. Koppel, I. A. Koppel, J. F. Kögel, J. Sundermeyer, U. Köhn, M. P. Coles and I. Leito, *J. Phys. Chem. A*, 2016, **120**, 2591–2604.

32 H. Wittmann, V. Raab, A. Schorm, J. Plackmeyer and J. Sundermeyer, *Eur. J. Inorg. Chem.*, 2001, 1937–1948.

33 A. B. Chaplin, J. A. Harrison and P. J. Dyson, *Inorg. Chem.*, 2005, **44**, 8407–8417.

34 M. Sauthier, F. Leca, R. Fernando de Souza, K. Bernardo-Gusmão, L. F. Trevisan Queiroz, L. Toupet and R. Réau, *New J. Chem.*, 2002, **26**, 630–635.

35 M. T. Reetz and E. Bohres, *Chem. Commun.*, 1998, 935–936.

36 M. J. Sgro and D. W. Stephan, *Dalton Trans.*, 2011, **40**, 2419–2421.

37 R. Cariou, F. Dahcheh, T. W. Graham and D. W. Stephan, *Dalton Trans.*, 2011, **40**, 4918–4925.

38 R. Cariou, T. W. Graham and D. W. Stephan, *Dalton Trans.*, 2013, **42**, 4237–4239.

39 R. Cariou, T. W. Graham, F. Dahcheh and D. W. Stephan, *Dalton Trans.*, 2011, **40**, 5419–5422.

40 T. Cheisson and A. Auffrant, *Dalton Trans.*, 2014, **43**, 13399–13409.

41 T. Cheisson, L. Mazaud and A. Auffrant, *Dalton Trans.*, 2018, **47**, 14521–14530.

42 M. J. Aroney, I. E. Buys, M. S. Davies and T. W. Hambley, *J. Chem. Soc., Dalton Trans.*, 1994, 2827–2834.

43 B. A. Arndtsen, H. F. Sleiman, L. McElwee-White and A. L. Rheingold, *Organometallics*, 1993, **12**, 2440–2444.

44 R. Tonner and G. Frenking, *Organometallics*, 2009, **28**, 3901–3905.

45 H. V. Huynh, *Chem. Rev.*, 2018, **118**, 9457–9492.

46 P. Imhoff, C. J. Elsevier and C. H. Stam, *Inorg. Chim. Acta*, 1990, **175**, 209–216.

47 M. J. Aroney, M. S. Davies, T. W. Hambley and R. K. Pierens, *J. Chem. Soc., Dalton Trans.*, 1994, 91–96.

48 C. X. Zhang, S. Kaderli, M. Costas, E. Kim, Y.-M. Neuhold, K. D. Karlin and A. D. Zuberbühler, *Inorg. Chem.*, 2003, **42**, 1807–1824.

49 B. R. James and R. J. P. Williams, *J. Chem. Soc.*, 1961, 2007–2019.

50 D. V Scaltrito, D. W. Thompson, J. A. O'Callaghan and G. J. Meyer, *Coord. Chem. Rev.*, 2000, **208**, 243–266.

51 G. D. Stroscio, R. D. Ribson and R. G. Hadt, *Inorg. Chem.*, 2019, **58**, 16800–16817.

52 L. Yan, Y. Lu and X. Li, *Phys. Chem. Chem. Phys.*, 2016, **18**, 5529–5536.